Spectrally selective emitters based on 3D Mo nanopillars for thermophotovoltaic energy harvesting

Anisha Chirumamilla [a, b], Yuanqing Yang [c], Maria H. Salazar [a], Fei Ding [c], Deyong Wang [b], Peter Kjær Kristensen [b], Peter Fojan [b], Sergey I. Bozhevolnyi [c], Duncan S. Sutherland [a], Kjeld Pedersen [b], Manohar Chirumamilla [b, d], *

[a] Interdisciplinary Nanoscience Center (iNANO) and iMAT, Aarhus University, Aarhus, 8000, Denmark
[b] Department of Materials and Production, Aalborg University, Skjernvej 4A, Aalborg Øst, 9220, Denmark
[c] Centre for Nano Optics, University of Southern Denmark, Campusvej 55, Odense, 5230, Denmark
[d] Institute of Optical and Electronic Materials, Hamburg University of Technology, Eissendorfer Strasse 38, Hamburg, 21073, Germany

ARTICLE INFO

ABSTRACT

High-temperature stable emitters with spectral selective functionality are an absolute condition for efficient conversion of thermal radiation into electricity using thermophotovoltaic (TPV) systems. Usually, spectral selective emitters are made up of multilayered materials or geometrical structures resulting from complex fabrication processes. Here, we report a spectrally selective emitter based on a single metal layer coating of molybdenum (Mo) over a 3D dielectric pillar geometry. 3D Mo nanopillars are fabricated using large-area and cost-effective hole-mask colloidal lithography. These nanostructures show an absorptivity/emissivity of 95% below the cut-off wavelength of an InGaAsSb PV cell at 2.25 μm, and a sharp decline in absorptivity/emissivity in the near-infrared regions, approaching a low emissivity of 10%. The 3D Mo nanopillars show outstanding thermal/structural stability up to 1473 K for 24 h duration under Ar atmosphere and polarization and angle invariance up to 60° incidence angles. With a low-cost and scalable fabrication method, 3D Mo nanostructures provide tremendous opportunities in TPV and high temperature photonic/plasmonic applications.

1. Introduction

Spectral selectivity of nanostructures with structural stability at high temperatures is of great importance in various applications in the fields of thermophotovoltaics (TPV), radiative cooling, energy-efficient lighting, photodetection and stray-light elimination [1−16]. In particular, nanostructures stable at temperatures higher than 1273 K and allowing of tailoring the thermal emission above the bandgap of the PV cell are essential in attaining high conversion efficiencies in TPV systems, using PV cells, such as InGaAsSb, GaSb, etc. In TPV, heat energy generated/collected from various sources is thermally coupled to an emitter. Where the emitter is designed to emit spectrally selective radiation to match the external quantum efficiency of the PV cell, and suppress the unabsorbable radiation with energies lower than the bandgap of the PV cell. Otherwise, the

unabsorbable radiation generates parasitic heat losses, which will heat up the PV cell housing, thereby reducing the PV cell efficiency. Ideal thermal emitters should show spectral selectivity with an emissivity $\varepsilon = 1$ for $E > E_g$ and $\varepsilon = 0$ for $E < E_g$, where E and E_g are the thermal photon energy and bandgap energy of the PV cell. Although theoretically TPV systems can provide efficiencies up to 85% [17], the maximum efficiency achieved so far is below 29% [18−21] due to the limited spectral selectivity and thermal stability of the nanostructures. According to the Stefan-Boltzmann law [22], a blackbody's radiative power is proportional to T^4. Thus, spectrally selective and thermally stable emitters play a critical role in obtaining high radiative power by operating the TPV systems at high temperatures.

Spectral selectivity can be obtained with various photonic/plasmonic nanostructures. To date, photonic crystals (PhCs) and metamaterials-based spectrally selective emitters have been widely investigated, where nanostructures were fabricated using electron beam or focused-ion beam lithography based patterning techniques. This is expensive and time-consuming, and it cannot be

* Corresponding author. Department of Materials and Production, Aalborg University, Skjernvej 4A, Aalborg Øst, 9220, Denmark.
E-mail address: mch@mp.aau.dk (M. Chirumamilla).

realized to a large-area fabrication at the wafer-scale level. In 3D PhCs, structures require complex fabrication steps and deep reactive ion etching of metals. Furthermore, PhCs only provide spectral selectivity at a narrow range of incidence angles [23], and 1D PhCs and hyperbolic metamaterial structures [24—26] require multiple layers of different materials. As the number of layers increases, emitters suffer from various degradation mechanisms. For instance, these structures suffer from delamination and internal stress, induced by different thermal expansion coefficients of the materials, and structural degradation can be observed after a few cycles of thermal annealing of the nanostructure. Arpin et al. [27] showed the fabrication of 3D PhCs coated with a protective HfO$_2$ layer for high temperature stability. These structures show excellent thermal and spectral stability up to 1273 K for 12 h. After annealing the structures at 1673 K for 1 h, an increment in the emissivity at the long-wavelength region is observed. Rinnerbauer et al. [28] showed the fabrication of Ta based 2D PhC absorber/emitter, to be operated at 1000 K, for solar TPV application. PhCs based structures provide sharp cut-off in absorptivity/emissivity at the bandgap of the PV cell. However, due to the lossy behaviour of the refractory Ta metal, compared to W or Mo, an increment in the emissivity is expected at operating temperatures higher than 1000 K. Li et al. [29] showed large-area selective solar absorbers for solar thermal energy conversion using Ni-based 3D nanopyramid arrays. Where these pyramids are covered with an anti-reflective coating to improve absorptivity. Thermal stability of the 3D nanopyramid structures was demonstrated up to 1073 K. Due to the low melting point of the Ni (~1700 K), these structures cannot be operated at high temperatures. Chang et al. [30] showed the lithography fabrication of refractory metasurfaces using metal-insulator-metal structures (coated with an anti-reflective coating) for TPV energy harvesting. These structures are stable up to 1473 K for 12 h operation. Cui et al. [31], showed W-carbon nanotube composite for TPV application, operating at 1273 K. However, these composite structures show increased emissivity at longer wavelengths after annealing for prolonged times. Moreover, 2D and 3D nanostructures contain sharp edges that are vulnerable to structural changes at high temperatures due to surface diffusion [6,32—37], where the surface diffusion rate is proportional to the gradient of the edge curvature [32]. Although refractory metals like W, Ta, ZrN and TiN [38—43] based nanostructures with protective coatings of Al$_2$O$_3$ or HfO$_2$ are used, spectrally selective emitters still suffer from delamination, diffusion and grain growth. Thus, developing thermally stable nanostructures with spectral selective functionality using large-area and cost-effective fabrication techniques remains a challenge, which hampers the deployment of efficient TPV systems over a large scale.

Herein, we demonstrate thermal stability of novel 3D Mo nanopillars based metamaterial structures, as spectrally selective emitters, fabricated by a large-area and low-cost patterning method (hole-mask colloidal lithography, HCL). With a melting point of ~2900 K, Mo based spectrally selective absorbers/emitters are used in high temperature applications [25,44—49]. Our design consists of a single metal layer of Mo with an 80 nm thickness over 3D Si structures to provide the required spectral selectivity. 3D Mo structures exhibit multiple electric resonances at the Mo/air and Mo/Si interfaces and magnetic resonances in the Si structure (Mie resonances), overall creating a broadband absorptivity in the visible-near infrared regions. A 230 nm height Mo nanopillar structure provides an emissivity of 95% between 0.99 and 1.85 μm, and a low emissivity of 5% in the near/mid-infrared regions. The bandwidth of the spectral selectivity can be easily tailored with the nanostructure height. Further, 3D Mo structures show angle/polarization-independent absorptivity/emissivity over a wide range of incidence angles, up to 60°, and outstanding thermal

stability up to 1473 K. A simple design of the 3D Mo structures with ease of scalable and low-cost fabrication method provide potential candidates for the development of high-efficiency TPV systems, and show a route to make thermally stable structures beyond 1473 K using refractory dielectric substrates such as Al$_2$O$_3$, MgO and HfO$_2$.

2. Results and discussion

A schematic presentation of the 3D Mo nanopillar structures is shown in Fig. 1(a), where D and H denote pillar diameter and height, of 300 nm and 230 nm, respectively, obtained from a FIB cut 3D Mo nanopillar (Inset of Fig. 1(c)). A 54° tilted view scanning electron micrograph (SEM) of the 3D Mo nanopillars is shown in Fig. 1(b and c). The inset of Fig. 1(c) shows the cross-sectional view of the 3D Mo nanopillar, where the Si pillar (marked with a white rectangular dashed box) is clearly seen. Fig. S1 addresses the challenges of large-area fabrication of the 3D Mo nanopillars, and the inset shows the top-view of the 3D Mo nanostructures. According to Kirchhoff's law of thermal radiation, the emissivity of a hot radiating body equals its absorptivity, thus, the TPV-relevant spectral emissivity is obtained by measuring the absorptivity. The optical absorptivity α is obtained by $\alpha = 1 - \rho - \tau$, where ρ and τ are reflectivity and transmissivity. Since $T = 0$ for an optically thick (80 nm) Mo film, the absorptivity α is directly obtained by the reflectivity: $\alpha = 1 - \rho$. Fig. 1(d) shows the absorptivity/emissivity spectrum of the 3D Mo nanopillars, which demonstrates above 90% absorptivity/emissivity in the 0.8—2 μm range and a rapid decrement after 2 μm. Fig. S2 shows the reflectivity spectra of 3D Si and Mo nanopillars. 3D Si nanopillars exhibit a low reflectivity of less than 20% below 1.1 μm and band-edge spectral characteristics at 1.1 μm due to the intrinsic nature of the indirect bandgap of the monocrystalline Si [50—52]. In comparison, 3D Mo nanopillars show a low reflectivity throughout the spectral region. The corresponding 54° tilted view SEM images are shown in the insets. Fig. S3(a) shows the typical absorptivity/emissivity spectra of the 3D Mo nanopillar structures at 230 nm and 1500 nm heights, and the corresponding SEM images are shown in Figs S3(b and c). Tailoring the 3D nanostructure height enables significant tunability of the spectral selectivity window.

Normal-incidence absorptivity/emissivity spectra of 3D Mo nanostructures for unpolarized, transverse-electric (TE) and transverse-magnetic (TM) polarizations are shown in Fig. 2(a), where the polarization-insensitive absorptivity/emissivity is observed throughout the spectral region. However, a slightly increased absorptivity/emissivity is observed in the visible wavelength regions for the unpolarized light. Fig. 2(b) shows the absorptivity/emissivity of the 3D Mo structures at 1.75 μm wavelength for oblique incidence angles, up to 80°. 3D Mo nanostructures show excellent angle insensitivity up to 65° oblique angle incidence. The invariance of the TE and TM polarization and oblique incidence angles up to 80° for the 230 nm height 3D Mo nanopillar structures is shown in Fig. 2(c and d) for 0.7 μm—2.2 μm wavelength range. The absorptivity/emissivity of the incident beam is above 90% within the spectral range of 0.8 μm—2.1 μm for the oblique incidence angles up to 65°, and then decreases to 50% for the oblique incidence angle of 80°. In the case of TM polarization, high absorptivity/emissivity is observed up to 60°, and then a gradual decrement in absorptivity/emissivity is observed.

Fig. 3(a) shows the absorptivity/emissivity spectra of the 3D Mo nanopillars measured at room temperature, before and after annealing at 1473 K for 24 h in an inert gas atmosphere at ambient pressure. After annealing the 3D Mo nanopillar structure for 24 h, the absorptivity/emissivity is significantly reduced up to 2 × after the cut-off wavelength λ_C at 2.25 μm (corresponding to the bandgap of InGaAsSb PV cell at 0.55 eV), see Fig. 3(a)-red solid trace. To
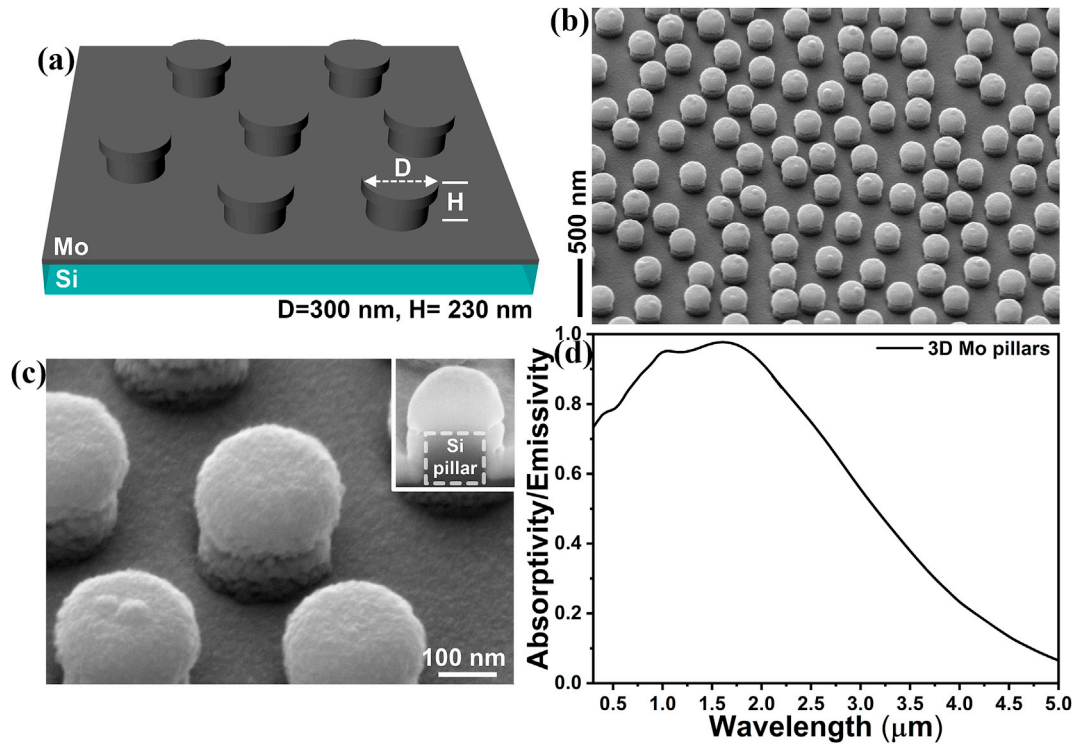
Fig. 1. (a) Schematic presentation of 3D Mo nanostructures. (b and c) SEM images at a 54° tilted view of the 3D Mo nanopillar structures. Inset of (c) shows the cross-sectional view of a single 3D Mo nanostructure depicted underneath the 3D Si pillar. (d) Absorptivity/emissivity spectra of the 3D Mo nanostructure.
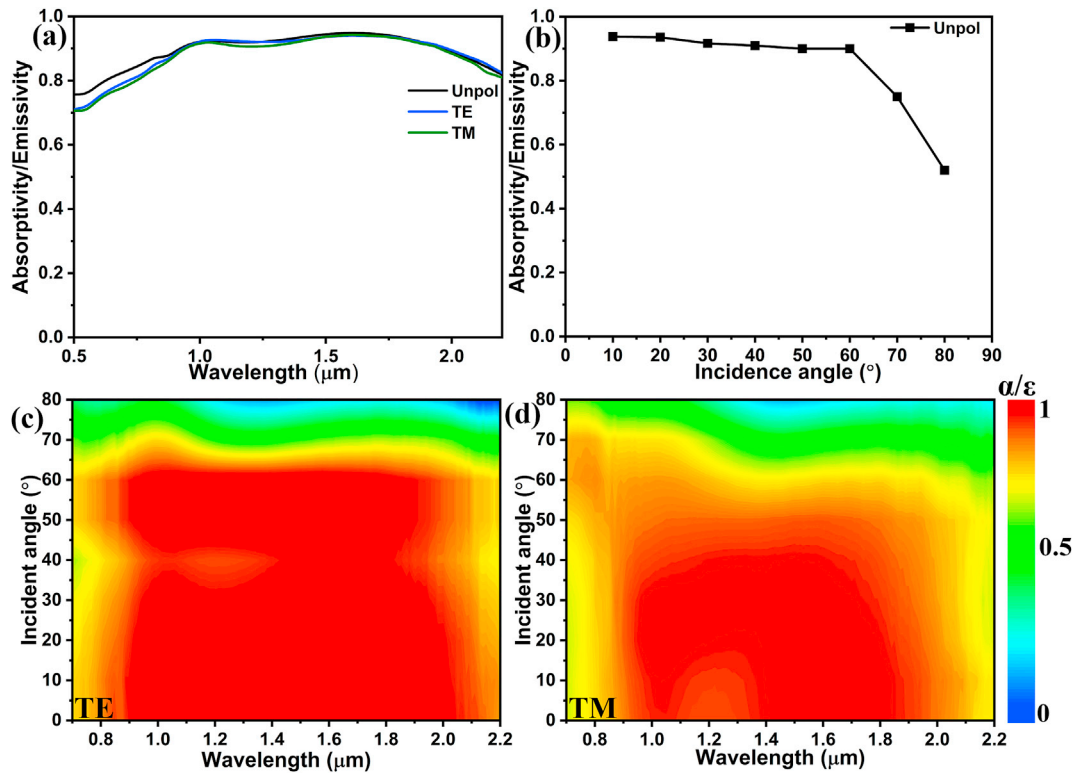

Fig. 2. (a) Experimental absorptivity/emissivity (α/ε) spectra of unpolarized, TE and TM polarized light at normal incidence. (b) Absorptivity/emissivity of the 3D Mo structure at 1.75 μm for various incidence angles. (c and d) Measured absorptivity/emissivity of 3D Mo nanostructures as a function of wavelength and incident angle for TE and TM polarizations.
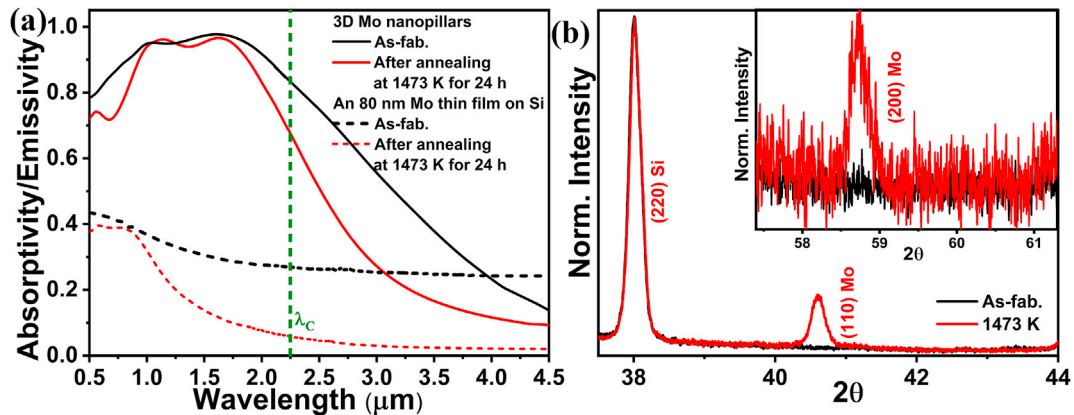
Fig. 3. (a) Experimental spectral selectivity of the 3D Mo nanostructured emitter taken at room temperature, before and after annealing at 1473 K for 24 h. λ_C represents the cut-off wavelength at 2.25 μm, corresponding to the InGaAsSb PV cell bandgap at 0.55 eV. Dashed lines represent the absorptivity/emissivity spectra of an 80 nm thick Mo film deposited on a planar Si substrate, before and after annealing at 1473 K for 24 h. The corresponding XRD patterns of the 80 nm thick Mo film are shown in (b).

understand the change in the spectral response of the 3D Mo nanopillars after annealing at 1473 K, an 80 nm thick Mo film is deposited on a planar Si substrate and annealed at 1473 K for 24 h. The absorptivity/emissivity spectrum of the as-prepared 80 nm thick planar film (black dashed line-Fig. 3(a)) shows absorptivity/emissivity of ~40% below 1 μm spectral region, and above the 1 μm wavelength range, it is decreased to 30%. Whereas the planar Mo film structure annealed at 1473 K shows a sharp decrement in absorptivity/emissivity above 1 μm region (Fig. 3(a) red dashed trace), where it changes from 30% to 5% in the near-mid infrared regions. This is in good agreement with the change in the Mo nanopillars absorptivity/emissivity after annealing at 1473 K. In order to investigate the changes in the absorptivity/emissivity due to the heat treatment at 1473 K, XRD, AFM and spectroscopic ellipsometry measurements are performed.

For the as-prepared 80 nm planar Mo film structure, XRD reflections (Fig. 3(b)) show no diffraction peaks for Mo, and only a Si reflex at (220) is observed, indicating that as-prepared planar Mo film is in the nanocrystalline state. However, after annealing the planar Mo structure at 1473 K for 24 h, strong reflexes of Mo at 2θ-angles of 40.6 and 58.7°, corresponding to (110) and (200), respectively, are observed, and that is in good agreement with the standard diffraction pattern of BCC Mo (JCPDS-01-1208), confirming the polycrystalline state of the Mo film. The surface morphology of the planar Mo film structure before and after annealing at 1473 K is investigated using AFM, and the respective images are shown in

Fig. 4(a and b). The as-prepared 80 nm thick planar Mo film contains smaller grains in the order of 10 nm, and after annealing the structure at 1473 K larger grains of 85 nm are formed, which confirms the transformation of nanocrystalline to the polycrystalline state that observed in the XRD measurements. The surface roughness of the as-prepared and annealed structures is 1 and 1.7 nm, respectively, and the influence of the surface roughness on the optical absorptivity was omitted [53,54]. Thus, the reduced absorptivity/emissivity of the 3D Mo nanostructures/planar films at longer wavelengths (Fig. 3(a)) is primarily due to the structural changes in Mo, from nanocrystalline to polycrystalline transformation upon the heat treatment.

Further, optical constants of the 80 nm thick Mo planar film structures, before and after annealing at 1473 K, are measured using spectroscopic ellipsometry. Fig. 5 shows the complex dielectric functions, real ε_1 and imaginary ε_2 parts of the permittivity, where ε_1 describes the polarizability of a material due to an external electric field and ε_2 represents ohmic and polarization losses in the material. The complex dielectric permittivities of the Mo thick planar film structure after annealing at high temperature are evaluated by fitting a Drude-Lorentz oscillator model (Eq. (1)) [55], where Drude and Lorentz terms represent the conduction electron contribution and interband transitions, respectively. The Drude term describes mainly the optical properties of the metal due to the free electrons contribution in the infrared range, whereas, the Lorentz term describes the interband transitions at the *d*-electronic
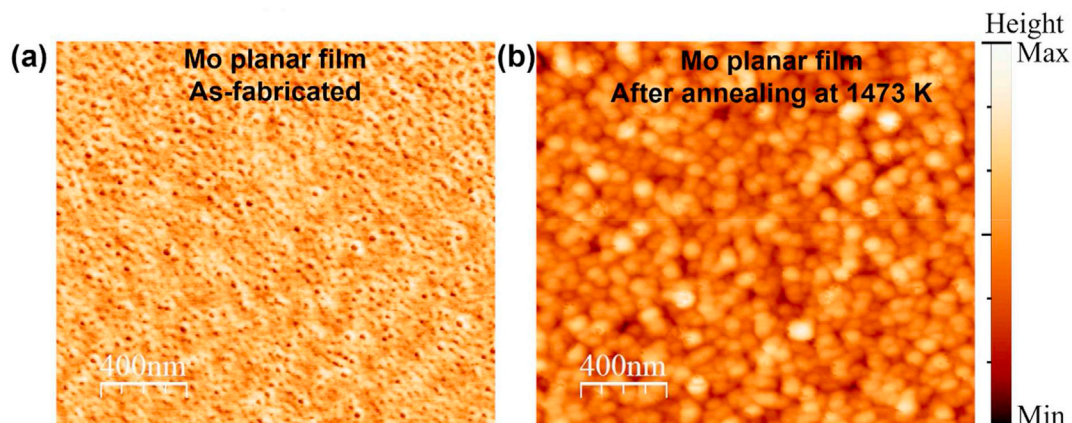

Fig. 4. (a and b) AFM images of the 80 nm thick Mo film for the as-fabricated, and after annealing at 1473 K for 24 h, respectively.
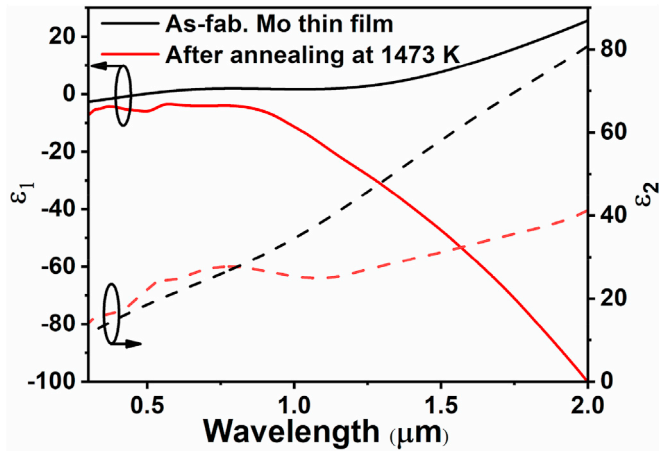
Fig. 5. Measured real and complex dielectric permittivities, ε_1 and ε_2, respectively, of an 80 nm Mo thin film structure, for the film as-fabricated and after annealing at 1473 K for 24 h.

bands in the UV−visible range,

$$\varepsilon(\omega) = \varepsilon_1 + i\varepsilon_2 = \varepsilon_\infty - \frac{\omega_p^2}{\omega^2 + i\Gamma_D\omega} + \sum_{j=1}^{5} \frac{A_j}{\omega_{0,j}^2 - \omega^2 - i\gamma_j\omega}, \quad (1)$$

Here, ε_∞, Γ_D, ω_p, $\omega_{0,j}$, A_j and γ_j are the background dielectric constant accounting for higher energy interband transitions outside the probed energy spectrum, collision frequency, plasma frequency, peak energy, strength and sharpness, respectively.

For the as-fabricated 80 nm thick Mo film, the real and imaginary parts of the complex dielectric functions are extracted using a wavelength-by-wavelength method [56], which is generally used for the materials when there is no prior knowledge of the material and dispersion relations are readily available. The complex dielectric functions are directly obtained from the ellipsometric parameters Ψ and Δ by extracting the real and imaginary parts numerically for each wavelength from the spectrum, and without the necessity to correlate with other wavelengths. This method was validated by performing the measurements at various angles between $50°$ and $70°$, and it provides identical optical constants for each angle.

The as-prepared Mo film exhibits a positive permittivity ε_1, and large ε_2, pointing that the as-prepared Mo film with nanocrystalline state behaves as a lossy metal. From the AFM image, the as-prepared Mo planar film structure contains a large number of small grains of the order of 10 nm. When the grain size is less than or of the order of the Mo electron mean free path (~11 nm) [57], the electron collision frequency will be increased due to grain boundary and surface scattering [58−60]. In turn, it increases the imaginary part of the permittivity and thereby optical losses. Thus, a high absorptivity/emissivity of 30% in the as-prepared nanocrystalline Mo film (Fig. 3(a)-black dashed trace) is observed in the near-mid infrared regions due to large ε_2 and positive ε_1. The optical constants of the Mo planar film structure after annealing at 1473 K exhibit negative ε_1 and low ε_2 (Fig. 5-red trace). This is the direct consequence of the polycrystalline state of Mo, and increased grain size (AFM images, Fig. 4(a and b)). When the grain size of Mo is in the order of 85 nm, it is much higher than the Mo electron mean free path. Thus, the effect of grain-boundary and surface scattering is insignificant, and the 80 nm thick Mo film behaves like a perfect bulk metal, contributing to the reduction of the near-infrared emissivity to 5%. In summary, a sharp decrement in absorptivity/emissivity of the 3D Mo nanopillars in the near-infrared region

(Fig. 3(a)-red solid trace) is attributed to the change in the optical constants of the Mo film.

Fig. 6 compares the spectral energy density of a blackbody radiator and 3D Mo nanopillars at 1473 K, which is normalized to the maximum value of the blackbody at 1473 K. The spectral energy density of the 3D Mo nanopillars is derived from the experimental absorptivity/emissivity spectrum, where the thermal radiation spectrum of 3D Mo nanostructures is obtained by multiplying the spectral radiation intensity of a blackbody at 1473 K and spectral emissivity of the 3D Mo nanostructures. The spectral radiance of a blackbody at 1473 K shows a maximal radiance in the infrared region with a high energy tail in the mid-infrared regions. This unabsorbable radiation (above λ_C) does not contribute to the electron-hole pair generation in the PV cell; instead, it will heat the PV cell housing and the PV cell, which in turn decreases the efficiency. Whereas, the 3D Mo nanopillars shows a significantly reduced spectral radiance above λ_C, leaving a very small percentage to radiate into free space, thereby avoiding the use of a cold-side selective optical filter between the emitter and PV cell [61]. The unwanted spectral energy density reduced by the 3D Mo nanopillars is shown with a red-colored area in Fig. 6.

To compare the spectral emission characteristics of 3D Mo nanopillars with that of a blackbody at the same temperature, we calculated the spectral efficiencies η for a blackbody and for 3D Mo nanopillars as a function of the temperature T and PV cell bandgap energy E_g (Fig. 7(a and b)). η is defined as the ratio of the convertible thermal radiation energy in the PV cell to the total thermal energy radiated by the emitter, as follows [28,62].

$$\eta = \int_{E_g}^{\infty} \frac{E_g}{E} \varepsilon(E) I_{BB}(E, T_{emitter})dE \bigg/ \int_0^\infty \varepsilon(E) I_{BB}(E, T_{emitter})dE \quad (2)$$

where ε, E, and I_{BB} are the spectral emissivity, photon energy and blackbody spectral power density at $T_{emitter}$, respectively. The blackbody exhibits 11% efficiency at 1073 K for a PV cell bandgap of 0.55 eV, which is raised to 25% when the blackbody temperature is increased to 1473 K. While 3D Mo nanopillars show 36% efficiency at 1073 K and approaching 50% at 1473 K for the same PV cell bandgap of 0.55 eV, which is 2 × higher. 3D Mo nanopillars show remarkable TPV spectral efficiency due to the sharp attenuation of the emissivity at near-mid infrared wavelength regions.
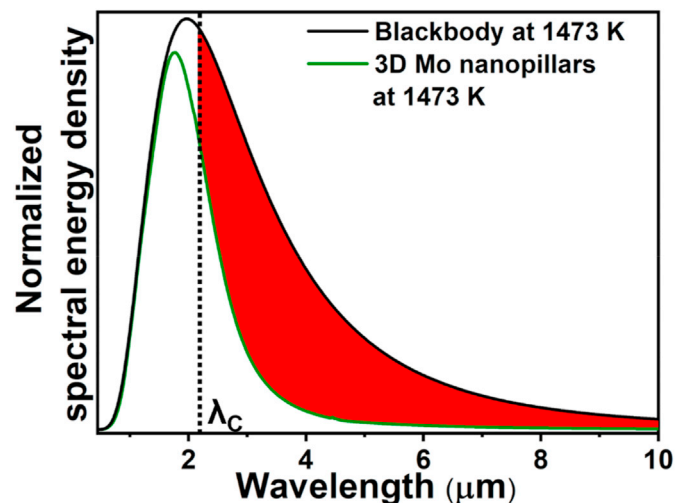

Fig. 6. Normalized spectral energy density of a blackbody radiator and 3D Mo nanopillar based spectrally selective emitter at 1473 K.
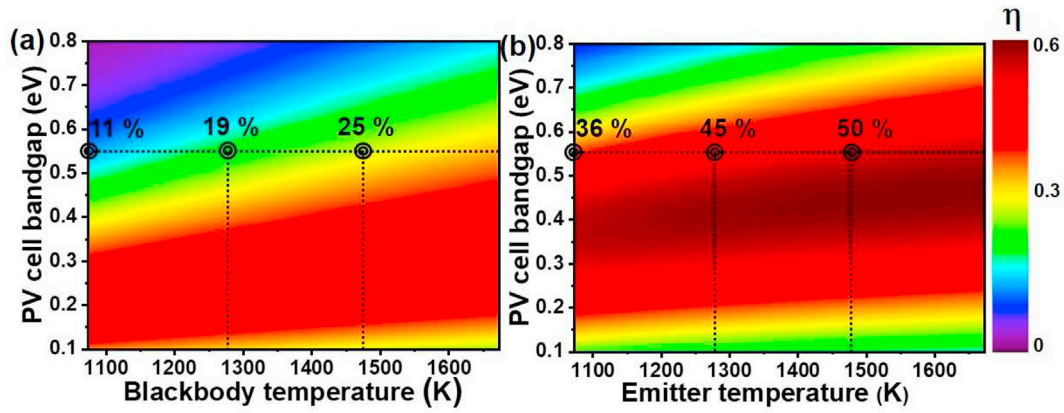
Fig. 7. (a and b) Contour maps show the calculated spectral efficiency *η*, of a blackbody radiator and 3D Mo nanopillar based spectrally selective emitter, respectively, for temperature versus PV cell bandgap energy.

Fig. 8(a) shows the calculated absorptivity of the 3D Mo nanopillar structure with 230 nm height using the finite-difference time-domain (FDTD) method. Here the optical constants of the planar Mo film measured after annealing at 1473 K are used in the calculations, and due to the lack of available optical constants data above 2 μm, the absorptivity/emissivity spectrum was calculated between 0.3 μm and 2 μm spectral range. A plane wave with *x*-polarization at normal-incidence is impinging on a 4 μm² unit-cell
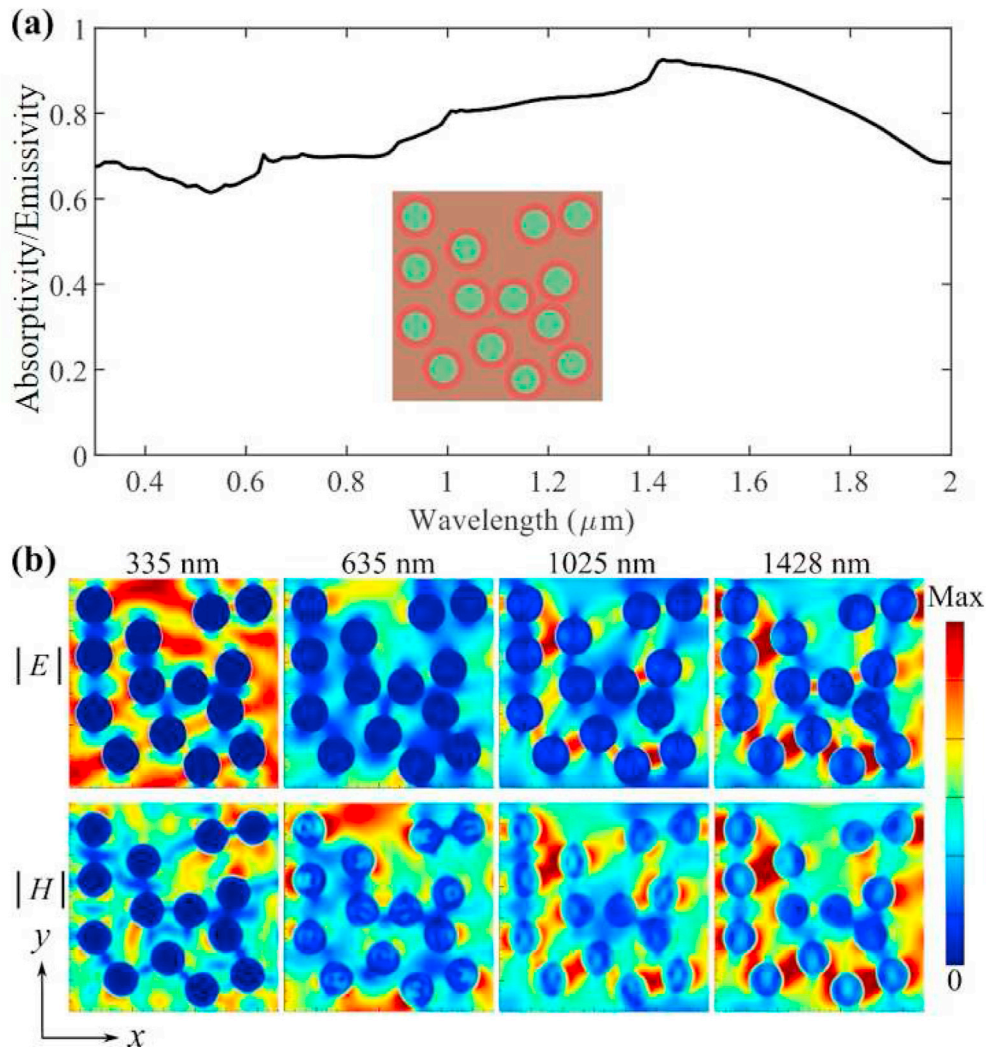

Fig. 8. (a) Calculated absorptivity spectrum of the 3D Mo nanopillar with 230 nm structure height. (b) Electric and magnetic field distributions at the *x-y* plane in 3D Mo nanopillar in a 4 μm² unit-cell containing 14 particles.

containing 14 Mo 3D nanopillars. The number of nanopillar structures in the unit-cell is obtained by measuring the particles in various spatial locations of the SEM image in Fig. S1. Further, the formation of the nanopillar positions on the x-y plane will lead to a negligible variance in absorptivity. Compared to the measured absorptivity/emissivity spectrum in Fig. 3(a) a reasonable agreement is observed between the simulated and measured spectra. To verify the absorption mechanism, the electric and magnetic field distributions of the various resonant modes are shown in Fig. 8(b). Generally speaking, the 3D metallic nanopillars generate multiple electric resonances at the metal/air and metal/Si interface, thereby creating horizontal cavities that trap and localize the propagating waves. Due to the highly lossy nature of Mo, the energy can be efficiently dissipated. At 1428 nm, strong electric and magnetic field localizations are observed between the nanopillars due to the coupling between them, which forms a lateral gap plasmon resonator. As shown in Fig. S4 and S5, this absorption peak is due to the collective effect of localized surface plasmon resonance of the top Mo layer of each individual nanopillar and the propagating surface plasmon resonance supported on the metal/Si interface. At 1025 nm, besides the propagating surface plasmon resonance supported on the metal/Si interface, there exists Mie resonance in the Si particles where magnetic fields are enhanced. The sharp absorption peak at 635 nm is more likely to be related to the Rayleigh mode effective periodicity of the randomly distributed particles (Fig. S4 and S5). At short wavelengths, such as $\lambda = 335$ nm, high-order localized surface plasmon resonances are supported around the Mo surfaces.

The thermal stability of the 3D Mo nanopillars is investigated under Ar atmosphere at ambient pressure. Fig. 9 shows the absorptivity/emissivity spectra of the 3D Mo nanostructures annealed at high temperatures up to 1523 K for 24 h duration. After annealing the 3D Mo nanostructures at 1273 K, the absorptivity/emissivity spectrum shows reduced emissivity in the near-infrared region, i.e., a sharp decline of the emissivity due to change in the crystallinity of the Mo structure, and it exhibits similar spectral characteristics up to the annealing temperature of 1473 K. SEM images of the 3D Mo nanostructures after annealing at 1423 K and 1473 K are shown in Fig. 10(a and b). No severe damage to the 3D Mo nanostructure is observed except grain growth in Mo due to nanocrystalline to polycrystalline structure transformation. Structural stability of the emitter is a crucial requirement to retain spectral selectivity at high temperatures. After annealing at 1523 K for 24 h, the absorptivity/emissivity is increased in the IR and visible to a level comparable to that of the as-prepared structure. At 1523 K, 3D Mo nanostructures show a reduced efficiency of 38% due to increased emissivity at long-wavelength regions, above the bandgap of the PV cell, due to structural degradation. The SEM image in Fig. 10(c) shows residual contamination on the 3D Mo nanopillar surface after annealing at 1523 K. To explore the underlying degradation mechanism after annealing at 1523 K, a focused ion beam (FIB) cross-section of the 3D Mo nanopillar is prepared. The inset of Fig. 10(c) shows a cross-sectional image of the 3D Mo nanopillar, where an arbitrary hole in the Si pillar geometry is observed. Fig. S6 shows that diffused Si material from the nanopillar is coming out as a residual Si nanowire. It is clear from the SEM images that the area under the 3D Si pillar diffuses faster than the area under the planar Si substrate. According to melting point depression, the melting point of the nanostructures is very much lower than their bulk counterpart materials [63]. Thus, it can be expected that Si nanopillars degrade faster at high temperatures than the planar Si substrate. It should be noted that 3D Mo nanostructures show excellent structural stability up to 1423 K, and structural degradation starts to appear at temperatures higher than 1473 K.

The experiments presented here demonstrate the limits of the thermal stability of the Mo structure and can be considered as accelerated degradation tests. It should be noted that, by decreasing the operating temperature of the emitter by 100 K, the emitter can show improved structural durability over 10 × due to the exponential temperature dependence of diffusion of atoms [24,26,64]. Fig. 7(b) shows that for an InGaAsSb PV cell, the TPV efficiency change from 45% to 50% by increasing the operating temperature from 1273 K to 1473 K, respectively. By considering the thermal losses at 1473 K due to the increased temperature difference between the TPV system and the surrounding environment and due to the hot-carriers, the emitter can be safely operated at 1273 K with a high TPV system efficiency for a prolonged duration. Further, at high temperatures, metals suffer from increased mean phonon number density in according to Bose-Einstein statistics [62], which increases the collision frequency and thereby optical losses in the structure. According to Xu et al. [55], the collision frequency of Mo increases with temperature linearly, from 0.08 eV to 0.26 eV, by changing the temperature from 273 K to 900 K, respectively. By extrapolating the collision frequencies up to 1273 K, 3D Mo nanostructures suffer from a 7% reduction in the emitter efficiency at high temperature operation of 1273 K due to thermal phonons.

A number of reported works on spectrally selective emitters show thermal stability up to temperatures of 1473 K for short durations [4,19,30,31,65]. Fig. 11 shows the calculated spectral efficiencies of the various emitter structures, using Eq. (2), reported elsewhere for operational temperature and PV cell bandgap of 1473 K and 0.55 eV, respectively. Chang et al. [30] demonstrated a W disc-based metasurface emitter for high temperature operation of 1473 K. However, the spectral efficiency of the emitter lies around 36% due to high residual absorptivity/emissivity at longer wavelength regions. The 3D PhC thermal emitter based on W coated colloidal crystals (Arpin et al. [27]) shows a spectral efficiency of 40% owing to the low reflectivity at the mid-infrared range. Woolf et al. [19] showed a W disc-based spectral emitter; in spite of high temperature stability, this structure exhibits a high emissivity above the cut-off wavelength of the PV cell, which results in a 41% spectral efficiency. Cui et al. [31], demonstrated a W-carbon nanotube composite-based PhC emitter, exhibiting around 44% spectral efficiency where the broadband spectral absorptivity of the carbon nanotubes contributed to the residual emissivity at longer wavelengths. Kim et al., and Chirumamilla et al. [26,65], demonstrated W−Al$_2$O$_3$, and W-HfO$_2$, respectively, based layered
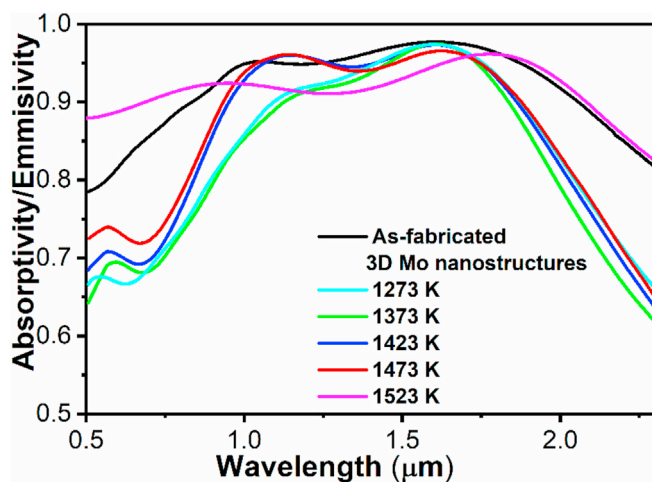

Fig. 9. Experimental absorptivity/emissivity spectra of the 3D Mo nanostructure taken at room temperature, and after annealing at high temperatures, up to 1523 K for 24 h duration.
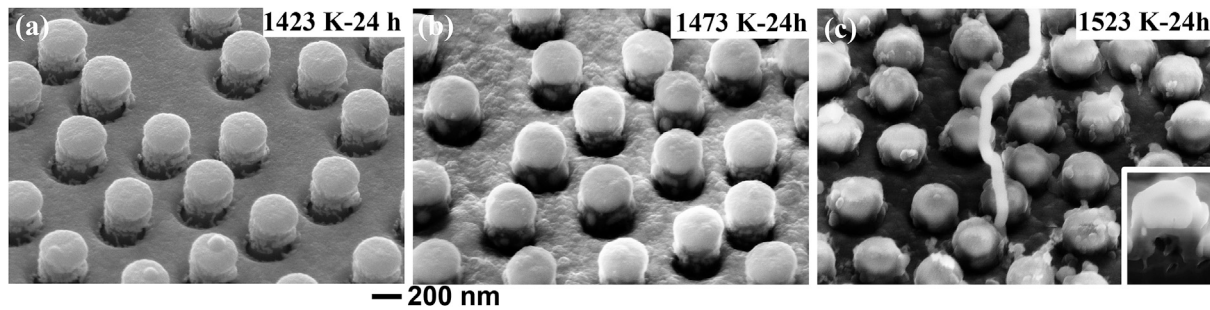
Fig. 10. a–c) SEM images at a 54°tilted view of the nanopillar structures after annealing at 1423 K, 1473 K and 1523 K for 24 h. All SEM images share the same scale bar. Inset of (c) shows a cross-sectional view of the 3D Mo nanopillar structure after annealing at 1523 K.
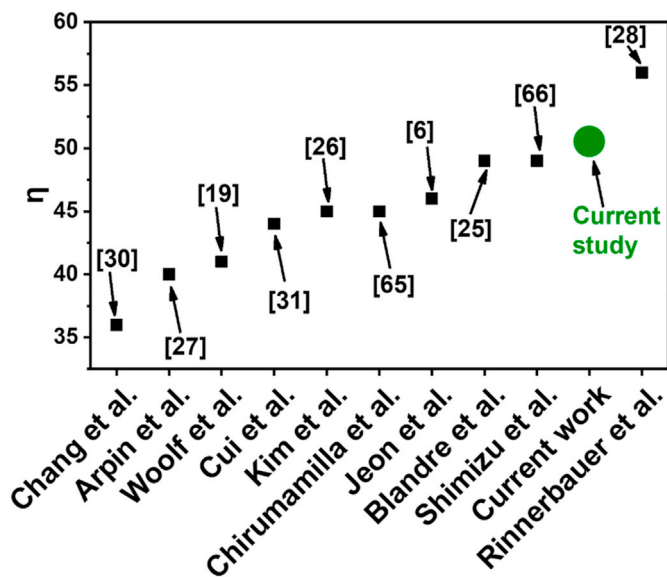

Fig. 11. Calculated spectral efficiencies of the selective emitters using references [6,19,25–28,30,31,65,66].

metamaterial structures as thermal emitters. These structures provide a spectral efficiency of 45%. Nevertheless, they suffer from structural degradation after a few cycles of heat treatment due to the internal stress induced by different thermal expansion co-efficients of the materials. Jeon et al. [6] showed W and TiAlN based selective emitters for high temperature operation of 1473 K, which exhibits a spectral efficiency of 46%. However, this structure emits strongly at longer wavelengths after exposure to high temperatures owing to the structural changes. Blandre et al., and Shimizu et al. [25,66] reported thermal emitters based on tri-layer structures of Mo and HfO_2, and W and YSZ, respectively. Albeit these structures provide a spectral efficiency of 49%, thermal stability over a long duration is an open question due to thin metallic layers with a thickness of 10 and 15 nm, where ultra-thin metal films suffer from melting point depression. Rinnerbauer et al. [28] showed 2D PhCs based emitter structures, which provide a high conversion effi-ciency of 56% due to a sharp cut-off of the absorptivity/emissivity at the bandgap of the PV cell. However, these structures are not stable at temperatures higher than 1473 K for prolonged durations, where the sharp corners and edges of the PhC structures act as hot-sites, and structural degradation occurs due to surface diffusion. Never-theless, PhCs provide the required spectral selectivity over a narrow range of oblique incidence angles. Further, all these emitters were fabricated using time-consuming lithography and etching pro-cesses or multilayer depositions of various materials. Whereas, the

3D Mo nanostructures of the present work provide a high spectral efficiency of 50%, and show a simple route to the fabrication of spectrally selective emitters with a single metal layer coating, where these nanostructures can be mass-produced to deploy the TPV systems over a large scale.

3. Conclusions

In summary, we have proposed a highly efficient and thermally stable spectrally selective emitter, based on a 3D Mo nanopillar structure, with a simple (containing only a single layer of Mo), low-cost and large-area fabrication method. The 3D Mo nanopillars exhibit polarization and wide-angle invariance absorptivity/emis-sivity. For a 230 nm height Mo nanopillar structure, the absorp-tivity/emissivity shows a peak maximum of 97% at 1.65 μm, stays above 90% between 0.8 and 2.0 μm, and 95% between 1 and 1.85 μm, and a low emissivity of ~5% in the mid-infrared region. Spectral selectivity of the structure can be tailored simply by changing the nanopillar height. The FDTD simulations demonstrate that the spectral selectivity is associated with gap-surface plas-mons of 3D Mo nanopillars and Mie resonances in the Si pillars. The thermal stability of the 3D Mo nanopillar structures is investigated at high temperatures. Under Ar atmosphere at ambient pressure, the 3D Mo nanopillars show excellent structural stability up to 1473 K. A 3D Mo nanopillar structures based emitter operating at 1473 K provides a TPV conversion efficiency of 50% by using an InGaAsSb PV cell. Above 1473 K, Si diffuses through Mo and de-grades the emitter structure. However, if the underlying Si material is replaced with refractory dielectric materials, such as, Al_2O_3, MgO or HfO_2, the thermal stability of the Mo film-based 3D emitters can be improved significantly beyond 1473 K, which is the topic for a future investigation. Our results open the door to the development of large-area and low-cost thermally stable spectrally selective emitters, that has tremendous application prospects in thermo-photovoltaics, infrared detectors and sources.

4. Material and methods

4.1. Selective emitter fabrication

The patterns of short-range ordered Cr nanodiscs with a thick-ness of ~20 nm are fabricated by HCL on a p-type Si (001) substrate. A detailed protocol of the fabrication procedure can be found elsewhere [67]. Afterwards, a typical RIE of Si is carried out using SF_6 (30 SCCM) + C_4F_8 (32 SCCM) at 1 mTorr. The process parameters temperature and power are held at 293 K, and 100 W, respectively, which yields an etch rate of approximately 100 nm/h. After achieving the required height of Si nanopillars, the Cr metal on the Si pillar is removed by commercially available chromium etch

(Sigma-Aldrich) solvent. Later, an 80 nm Mo film is deposited onto the Si pillars by direct current (DC) magnetron sputter deposition at a base pressure of 5×10^{-6}. Ar gas of 20 SCCM is let into the chamber, and bias of 100 W is applied for DC sputtering, which yields a deposition rate of 0.3 nm/s. All SEM images are taken by a Zeiss 1540 XB machine.

4.2. Finite-difference time-domain simulations

A commercial software (FDTD Solution, Lumerical Inc., Vancouver, Canada) is used to simulate optical properties (far- and near-field) of the 3D Mo nanopillar structures. The optical constants of deposited Mo film are taken from ellipsometry measurements (Semilab SE2000) in the optical range of $300-2000$ nm with an incident angle of $70°$, and implemented in the Lumerical simulations. For Si, the optical constants are adopted from Wood et al. [68]. A 5 nm mesh grid size is used all over the simulation region, and the incident plane wave source is polarized along the x-direction. In the case of a single Mo nanopillar, perfectly matched layer (PML) absorbing boundary conditions are applied at all the simulation domain boundaries. For arrays and short-range ordered nanostructures, periodic boundary conditions are used along the x- and y-directions while PML boundary condition is applied along the z-direction.

4.3. Absorptivity/emissivity measurements

Optical properties of the spectrally selective 3D Mo nanopillar structures in the visible and near-infrared are measured using a PerkinElmer Lambda 1050 spectrometer with a 150 mm integrating sphere. The incident light is unpolarized, and the minimum angle of incidence of the system is $8°$. Reflectivity measurements are performed in the optical range of $300-2300$ nm with a wavelength scan step of 5 nm, and a labsphere spectralon reflectance standard is used for normalization. Glan-Taylor air-spaced polarizers are used to investigate the polarization sensitivity of the 3D Mo nanopillars. The angular sensitivity of the nanostructures is measured with a variable angle reflectance center mount holder, which is attached to the integrating sphere. A PerkinElmer Spectrum One FTIR spectrometer is used to perform mid-infrared absorptivity/emissivity measurements.

4.4. Thermal stability

Thermal annealing experiments are performed in a tube furnace. After loading the sample, a rough vacuum pump is used to obtain mTorr level vacuum before introducing the forming gas (5% H_2 and 95% Ar) and continued to flow during annealing the structures at high temperatures for a 24 h period. The temperature is ramped at a rate of $10 °C$ min^{-1}.

Declaration of competing interest

The authors declare that they have no known competing financial interests or personal relationships that could have appeared to influence the work reported in this paper.

Acknowledgements

Appendix A. Supplementary data

Supplementary data to this article can be found online at https://doi.org/10.1016/j.mtphys.2021.100503.

Credit author statement

Anisha Chirumamilla: Writing the manuscript, **Anisha Chirumamilla**, **Maria H. Salazar and Duncan S. Sutherland**: Design, fabrication and characterization of 3D Mo nanostructures, **Yuanqing Yang and Fei Ding**: FDTD simulations, **Deyong Wang, Peter Kjær Kristensen and Peter Fojan**: Meteorology, **Duncan S. Sutherland**, **Sergey** I. **Bozhevolnyi, Kjeld Pedersen and Manohar Chirumamilla**: Conceptualization, reviewing and editing the manuscript.

Supporting information

Supplementary data associated with this article can be found in the online https://doi.org/

References

[1] W. Li, U. Guler, N. Kinsey, G.V. Naik, A. Boltasseva, J. Guan, V.M. Shalaev, A.V. Kildishev, Refractory plasmonics with titanium nitride: broadband metamaterial absorber, Adv. Mater. 26 (2014) 7959.

[2] Y. Kim, M.-J. Kim, Y.-S. Kim, H. Lee, S.-M. Lee, Nanostructured radiation emitters: design rules for high-performance thermophotovoltaic systems, ACS Photonics 6 (2019) 2260.

[3] M. Suemitsu, T. Asano, T. Inoue, S. Noda, High-efficiency thermophotovoltaic system that employs an emitter based on a silicon rod-type photonic crystal, ACS Photonics 7 (2020) 80.

[4] T. Burger, C. Sempere, B. Roy-Layinde, A. Lenert, Present efficiencies and future opportunities in thermophotovoltaics, Joule 4 (2020) 1660.

[5] G.T. Papadakis, S. Buddhiraju, Z. Zhao, B. Zhao, S. Fan, Broadening near-field emission for performance enhancement in thermophotovoltaics, Nano Lett. 20 (2020) 1654.

[6] N. Jeon, D.J. Mandia, S.K. Gray, J.J. Foley, A.B.F. Martinson, High-temperature selective emitter design and materials: titanium aluminum nitride alloys for thermophotovoltaics, ACS Appl. Mater. Interfaces 11 (2019) 41347.

[7] M. Chirumamilla, A.S. Roberts, F. Ding, D. Wang, P.K. Kristensen, S.I. Bozhevolnyi, K. Pedersen, Multilayer tungsten-alumina-based broadband light absorbers for high-temperature applications, Opt. Mater. Express 6 (2016) 2704.

[8] Y. Li, W. Li, T. Han, X. Zheng, J. Li, B. Li, S. Fan, C.-W. Qiu, Transforming heat transfer with thermal metamaterials and devices, Nat. Rev. Mater. 6 (2021) 488.

[9] A. Datas, R. Vaillon, Thermionic-enhanced near-field thermophotovoltaics, Nanomater. Energy 61 (2019) 10.

[10] B. Zhao, K. Chen, S. Buddhiraju, G. Bhatt, M. Lipson, S. Fan, High-performance near-field thermophotovoltaics for waste heat recovery, Nanomater. Energy 41 (2017) 344.

[11] A.S. Rana, M. Zubair, A. Danner, M.Q. Mehmood, Revisiting tantalum based nanostructures for efficient harvesting of solar radiation in STPV systems, Nanomater. Energy 80 (2021) 105520.

[12] Z. Wu, J. Wang, Y. Liu, S. Hou, X. Liu, Q. Zhang, F. Cao, A review of spectral controlling for renewable energy harvesting and conserving, Mater. Today Phys. 18 (2021) 100388.

[13] T. Krekeler, S.S. Rout, G.V. Krishnamurthy, M. Störmer, M. Arya, A. Ganguly, D.S. Sutherland, S.I. Bozhevolnyi, M. Ritter, K. Pedersen, A.Y. Petrov, M. Eich, M. Chirumamilla, Unprecedented thermal stability of plasmonic titanium nitride films up to 1400 °C, Adv. Opt. Mater. (2021) 2100323, https://doi.org/10.1002/adom.202100323.

[14] A.S. Roberts, M. Chirumamilla, K. Thilsing-Hansen, K. Pedersen, S.I. Bozhevolnyi, Near-infrared tailored thermal emission from wafer-scale continuous-film resonators, Opt Express 23 (2015) A1111.

[15] A.S. Roberts, T. Søndergaard, M. Chirumamilla, A. Pors, J. Beermann, K. Pedersen, S.I. Bozhevolnyi, Light extinction and scattering from individual and arrayed high-aspect-ratio trenches in metals, Phys. Rev. B 93 (2016): 075413.

[16] P.N. Dyachenko, S. Molesky, A. Yu Petrov, M. Störmer, T. Krekeler, S. Lang, M. Ritter, Z. Jacob, M. Eich, Controlling thermal emission with refractory epsilon-near-zero metamaterials via topological transitions, Nat. Commun. 7 (2016) 11809.

[17] N.-P. Harder, P. Würfel, Theoretical limits of thermophotovoltaic solar energy

conversion, Semicond. Sci. Technol. 18 (2003) S151.

[18] A. Datas, A. Martí, Thermophotovoltaic energy in space applications: review and future potential, Sol. Energy Mater. Sol. Cells 161 (2017) 285.

[19] D.N. Woolf, E.A. Kadlec, D. Bethke, A.D. Grine, J.J. Nogan, J.G. Cederberg, D. Bruce Burckel, T.S. Luk, E.A. Shaner, J.M. Hensley, High-efficiency thermo-photovoltaic energy conversion enabled by a metamaterial selective emitter, Optica 5 (2018) 213.

[20] A. Lenert, D.M. Bierman, Y. Nam, W.R. Chan, I. Celanović, M. Soljačić, E.N. Wang, A nanophotonic solar thermophotovoltaic device, Nat. Nano-technol. 9 (2014) 126.

[21] Z. Omair, G. Scranton, L.M. Pazos-Outón, T.P. Xiao, M.A. Steiner, V. Ganapati, P.F. Peterson, J. Holzrichter, H. Atwater, E. Yablonovitch, Ultraefficient ther-mophotovoltaic power conversion by band-edge spectral filtering, Proc. Natl. Acad. Sci. Unit. States Am. 116 (2019) 15356.

[22] D. Chubb, Fundamentals of Thermophotovoltaic Energy Conversion, Elsevier Science, 2007.

[23] M. Garín, D. Hernández, T. Trifonov, R. Alcubilla, Three-dimensional metallo-dielectric selective thermal emitters with high-temperature stability for thermophotovoltaic applications, Sol. Energy Mater. Sol. Cells 134 (2015) 22.

[24] M. Chirumamilla, G.V. Krishnamurthy, K. Knopp, T. Krekeler, M. Graf, D. Jalas, M. Ritter, M. Störmer, A.Y. Petrov, M. Eich, Metamaterial emitter for ther-mophotovoltaics stable up to 1400 °C, Sci. Rep. 9 (2019) 7241.

[25] E. Blandre, M. Shimizu, A. Kohiyama, H. Yugami, P.-O. Chapuis, R. Vaillon, Spectrally shaping high-temperature radiators for thermophotovoltaics using Mo-HfO$_2$ trilayer-on-substrate structures, Opt Express 26 (2018) 4346.

[26] M. Chirumamilla, G.V. Krishnamurthy, S.S. Rout, M. Ritter, M. Störmer, A.Y. Petrov, M. Eich, Thermal stability of tungsten based metamaterial emitter under medium vacuum and inert gas conditions, Sci. Rep. 10 (2020) 3605.

[27] K.A. Arpin, M.D. Losego, A.N. Cloud, H. Ning, J. Mallek, N.P. Sergeant, L. Zhu, Z. Yu, B. Kalanyan, G.N. Parsons, G.S. Girolami, J.R. Abelson, S. Fan, P.V. Braun, Three-dimensional self-assembled photonic crystals with high temperature stability for thermal emission modification, Nat. Commun. 4 (2013) 2630.

[28] V. Rinnerbauer, A. Lenert, D.M. Bierman, Y.X. Yeng, W.R. Chan, R.D. Geil, J.J. Senkevich, J.D. Joannopoulos, E.N. Wang, M. Soljačić, I. Celanovic, Metallic photonic crystal absorber-emitter for efficient spectral control in high-temperature solar thermophotovoltaics, Adv. Energy Mater. 4 (2014) 1400334.

[29] P. Li, B. Liu, Y. Ni, K.K. Liew, J. Sze, S. Chen, S. Shen, Large-scale nanophotonic solar selective absorbers for high-efficiency solar thermal energy conversion, Adv. Mater. 27 (2015) 4585.

[30] C.-C. Chang, W.J.M. Kort-Kamp, J. Nogan, T.S. Luk, A.K. Azad, A.J. Taylor, D.A.R. Dalvit, M. Sykora, H.-T. Chen, High-temperature refractory meta-surfaces for solar thermophotovoltaic energy harvesting, Nano Lett. 18 (2018) 7665.

[31] K. Cui, P. Lemaire, H. Zhao, T. Savas, G. Parsons, A.J. Hart, Tungsten−carbon nanotube composite photonic crystals as thermally stable spectral-selective absorbers and emitters for thermophotovoltaics, Adv. Energy Mater. 8 (2018) 1801471.

[32] D. Peykov, Y.X. Yeng, I. Celanovic, J.D. Joannopoulos, C.A. Schuh, Effects of surface diffusion on high temperature selective emitters, Opt Express 23 (2015) 9979.

[33] V. Rinnerbauer, Y.X. Yeng, W.R. Chan, J.J. Senkevich, J.D. Joannopoulos, M. Soljačić, I. Celanovic, High-temperature stability and selective thermal emission of polycrystalline tantalum photonic crystals, Opt Express 21 (2013) 11482.

[34] F. Cao, D. Kraemer, L. Tang, Y. Li, A.P. Litvinchuk, J. Bao, G. Chen, Z. Ren, A high-performance spectrally-selective solar absorber based on a yttria-stabilized zirconia cermet with high-temperature stability, Energy Environ. Sci. 8 (2015) 3040.

[35] R. Zhang, J. Cohen, S. Fan, P.V. Braun, Electrodeposited high strength, ther-mally stable spectrally selective rhenium nickel inverse opals, Nanoscale 9 (2017) 11187.

[36] J.B. Chou, Y.X. Yeng, Y.E. Lee, A. Lenert, V. Rinnerbauer, I. Celanovic, M. Soljačić, N.X. Fang, E.N. Wang, S.-G. Kim, Enabling ideal selective solar absorption with 2D metallic dielectric photonic crystals, Adv. Mater. 26 (2014) 8041.

[37] V. Rinnerbauer, S. Ndao, Y.X. Yeng, W.R. Chan, J.J. Senkevich, J.D. Joannopoulos, M. Soljacic, I. Celanovic, Recent developments in high-temperature photonic crystals for energy conversion, Energy Environ. Sci. 5 (2012) 8815.

[38] J.H. Park, S.E. Han, P. Nagpal, D.J. Norris, Observation of thermal beaming from tungsten and molybdenum bull's eyes, ACS Photonics 3 (2016) 494.

[39] Y. Li, C. Lin, D. Zhou, Y. An, D. Li, C. Chi, H. Huang, S. Yang, C.Y. Tso, C.Y.H. Chao, B. Huang, Scalable all-ceramic nanofilms as highly efficient and thermally stable selective solar absorbers, Nanomater. Energy 64 (2019) 103947.

[40] N.R. Denny, S.E. Han, D.J. Norris, A. Stein, Effects of thermal processes on the structure of monolithic tungsten and tungsten alloy photonic crystals, Chem. Mater. 19 (2007) 4563.

[41] N.R. Denny, F. Li, D.J. Norris, A. Stein, In situ high temperature TEM analysis of sintering in nanostructured tungsten and tungsten−molybdenum alloy pho-tonic crystals, J. Mater. Chem. 20 (2010) 1538.

[42] M. Chirumamilla, A. Chirumamilla, Y. Yang, A.S. Roberts, P.K. Kristensen, K. Chaudhuri, A. Boltasseva, D.S. Sutherland, S.I. Bozhevolnyi, K. Pedersen, Large-area ultrabroadband Absorber for solar thermophotovoltaics based on 3D titanium nitride nanopillars, Adv. Opt. Mater. 5 (2017) 1700552.

[43] A.S. Roberts, M. Chirumamilla, D. Wang, L. An, K. Pedersen, N.A. Mortensen, S.I. Bozhevolnyi, Ultra-thin titanium nitride films for refractory spectral selectivity [Invited], Opt. Mater. Express 8 (2018) 3717.

[44] J.-Z. Lu, B.-H. Chen, L.-H. Jin, Z. Fang, G. Liu, X.-H. Gao, Thermal stability investigation of the SS/MO/Al$_2$O$_3$ spectrally selective solar absorber coatings, Surf. Eng. 35 (2019) 565.

[45] M. Pan, Q. Li, Y. Hong, L. Cai, J. Lu, M. Qiu, Circular-polarization-sensitive ab-sorption in refractory metamaterials composed of molybdenum zigzag arrays, Opt Express 26 (2018) 17772.

[46] A. Kohiyama, M. Shimizu, H. Yugami, Unidirectional radiative heat transfer with a spectrally selective planar absorber/emitter for high-efficiency solar thermophotovoltaic systems, APEX 9 (2016) 112302.

[47] N.P. Sergeant, O. Pincon, M. Agrawal, P. Peumans, Design of wide-angle solar-selective absorbers using aperiodic metal-dielectrvic stacks, Opt Express 17 (2009) 22800.

[48] R. Sakakibara, V. Stelmakh, W.R. Chan, M. Ghebrebrhan, J.D. Joannopoulos, M. Soljacic, I. Čelanović, Practical emitters for thermophotovoltaics: a review, J. Photon. Energy 9 (2019): 032713.

[49] T. Yokoyama, T.D. Dao, K. Chen, S. Ishii, R.P. Sugavaneshwar, M. Kitajima, T. Nagao, Spectrally selective mid-infrared thermal emission from molybde-num plasmonic metamaterial operated up to 1000 °C, Adv. Opt. Mater. 4 (2016) 1987.

[50] U. Guler, A.V. Kildishev, A. Boltasseva, V.M. Shalaev, Plasmonics on the slope of enlightenment: the role of transition metal nitrides, Faraday Discuss 178 (2015) 71.

[51] H. Tian, Z. Zhou, T. Liu, C. Karina, U. Guler, V. Shalaev, P. Bermel, High tem-perature efficient, stable Si wafer-based selective solar absorbers, Appl. Phys. Lett. 110 (2017) 141101.

[52] T. Asano, M. Suemitsu, K. Hashimoto, M. De Zoysa, T. Shibahara, T. Tsutsumi, S. Noda, Near-infrared−to−visible highly selective thermal emitters based on an intrinsic semiconductor, Sci. Adv. 2 (2016): e1600499.

[53] K.M. McPeak, S.V. Jayanti, S.J.P. Kress, S. Meyer, S. Iotti, A. Rossinelli, D.J. Norris, Plasmonic films can easily Be better: rules and recipes, ACS Photonics 2 (2015) 326.

[54] J.H. Park, P. Ambwani, M. Manno, N.C. Lindquist, P. Nagpal, S.-H. Oh, C. Leighton, D.J. Norris, Single-crystalline silver films for plasmonics, Adv. Mater. 24 (2012) 3988.

[55] M. Xu, J.-Y. Yang, L. Liu, Temperature-dependent dielectric functions of bcc transition metals Cr, Mo, and W from ultraviolet to infrared regions: a theo-retical and experimental study, J. Appl. Phys. 123 (2018) 155102.

[56] H.G. Tompkins, E.A. Irene, Handbook of Ellipsometry, William Andrew, 2005.

[57] D. Gall, Electron mean free path in elemental metals, J. Appl. Phys. 119 (2016): 085101.

[58] G. Ding, C. Clavero, D. Schweigert, M. Le, Thickness and microstructure effects in the optical and electrical properties of silver thin films, AIP Adv. 5 (2015) 117234.

[59] R. Henriquez, L. Moraga, G. Kremer, M. Flores, A. Espinosa, R.C. Munoz, Size effects in thin gold films: discrimination between electron-surface and electron-grain boundary scattering by measuring the Hall effect at 4 K, Appl. Phys. Lett. 102 (2013): 051608.

[60] E.-T. Hu, Q.-Y. Cai, R.-J. Zhang, Y.-F. Wei, W.-C. Zhou, S.-Y. Wang, Y.-X. Zheng, W. Wei, L.-Y. Chen, Effective method to study the thickness-dependent dielectric functions of nanometal thin film, Opt. Lett. 41 (2016) 4907.

[61] T. Burger, D. Fan, K. Lee, S.R. Forrest, A. Lenert, Thin-film architectures with high spectral selectivity for thermophotovoltaic cells, ACS Photonics 5 (2018) 2748.

[62] T. Bauer, Thermophotovoltaics: Basic Principles and Critical Aspects of System Design, Springer Science & Business Media, 2011.

[63] J.P. Borel, Thermodynamical size effect and the structure of metallic clusters, Surf. Sci. 106 (1981) 1.

[64] G.V. Krishnamurthy, M. Chirumamilla, S.S. Rout, K.P. Furlan, T. Krekeler, M. Ritter, H.-W. Becker, A.Y. Petrov, M. Eich, M. Störmer, Structural degra-dation of tungsten sandwiched in hafnia layers determined by in-situ XRD up to 1520 °C, Sci. Rep. 11 (2021) 3330.

[65] J.H. Kim, S.M. Jung, M.W. Shin, Thermal degradation of refractory layered metamaterial for thermophotovoltaic emitter under high vacuum condition, Opt Express 27 (2019) 3039.

[66] M. Shimizu, A. Kohiyama, H. Yugami, High-efficiency solar-thermophotovoltaic system equipped with a monolithic planar selective absorber/emitter, J. Photon. Energy 5 (2015): 053099.

[67] H. Fredriksson, Y. Alaverdyan, A. Dmitriev, C. Langhammer, D.S. Sutherland, M. Zäch, B. Kasemo, Hole−mask colloidal lithography, Adv. Mater. 19 (2007) 4297.

[68] D.L. Wood, K. Nassau, T.Y. Kometani, D.L. Nash, Optical properties of cubic hafnia stabilized with yttria, Appl. Opt. 29 (1990) 604.